

See discussions, stats, and author profiles for this publication at: <https://www.researchgate.net/publication/264865842>

Composite Photothermal Platform of Polypyrrole-Enveloped Fe₃O₄ Nanoparticle Self-Assembled Superstructures

ARTICLE in ACS APPLIED MATERIALS & INTERFACES · AUGUST 2014

Impact Factor: 6.72 · DOI: 10.1021/am503831m · Source: PubMed

CITATIONS

18

READS

30

8 AUTHORS, INCLUDING:



Xue Zhang

Xinjiang University

26 PUBLICATIONS 289 CITATIONS

SEE PROFILE



Hao Zhang

North Sichuan Medical College

264 PUBLICATIONS 4,601 CITATIONS

SEE PROFILE



Sun Hongchen

Jilin University

85 PUBLICATIONS 1,441 CITATIONS

SEE PROFILE



Yang Bai

Iowa State University

446 PUBLICATIONS 9,338 CITATIONS

SEE PROFILE

Composite Photothermal Platform of Polypyrrole-Enveloped Fe₃O₄ Nanoparticle Self-Assembled Superstructures

Xue Zhang,[†] Xiaowei Xu,[‡] Tingting Li,[†] Min Lin,[†] Xiaoying Lin,[†] Hao Zhang,^{*,†} Hongchen Sun,^{*,‡} and Bai Yang[†]

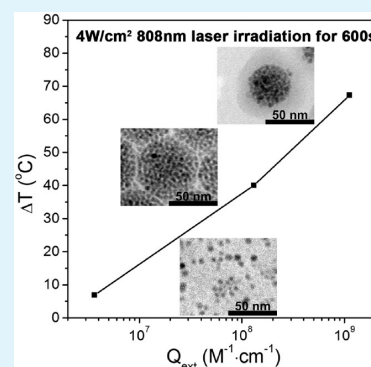
[†]State Key Laboratory of Supramolecular Structure and Materials, College of Chemistry, Jilin University, Changchun 130012, People's Republic of China

[‡]School of Stomatology, Jilin University, Changchun 130041, People's Republic of China

S Supporting Information

ABSTRACT: Photothermal nanoplatforms with small size, low cost, multifunctionality, good biocompatibility and in particular biodegradability are greatly desired in the exploration of novel diagnostic and therapeutic methodologies. Despite Fe₃O₄ nanoparticles (NPs) have been approved as safe clinical agents, the low molar extinction coefficient and subsequent poor photothermal performance shed the doubt as effective photothermal materials. In this paper, we demonstrate the fabrication of polypyrrole (PPy)-enveloped Fe₃O₄ NP superstructures with a spherical morphology, which leads to a 300-fold increase in the molar extinction coefficient. The basic idea is the optimization of Fe₃O₄ electronic structures. By controlling the self-assembly of Fe₃O₄ NPs, the diameters of the superstructures are tuned from 32 to 64 nm. This significantly enhances the indirect transition and magnetic coupling of Fe ions, thus increasing the molar extinction coefficient of Fe₃O₄ NPs from 3.65×10^6 to 1.31×10^8 M⁻¹ cm⁻¹ at 808 nm. The envelopment of Fe₃O₄ superstructures with conductive PPy shell introduces additional electrons in the Fe₃O₄ oscillation system, and therewith further enhances the molar extinction coefficient to 1.12×10^9 M⁻¹ cm⁻¹. As a result, the photothermal performance is greatly improved. Primary cell experiments indicate that PPy-enveloped Fe₃O₄ NP superstructures are low toxic, and capable to kill Hela cells under near-infrared laser irradiation. Owing to the low cost, good biocompatibility and biodegradability, the PPy-enveloped Fe₃O₄ NP superstructures are promising photothermal platform for establishing novel diagnostic and therapeutic methods.

KEYWORDS: nanocomposites, photothermal platform, polypyrrole, Fe₃O₄, self-assembly



1. INTRODUCTION

Photothermal nanoplatforms defined as biocompatible nano-architectures with good photothermal conversion behavior and subsequent heat-related functionalities have attracted increasing interest owing to the current exploration of novel diagnostic and therapeutic methodologies.^{1,2} Such platforms can be directly employed as thermal therapeutic agents to treat diseases, for example, the ablation of cancer cells by near-infrared (NIR) laser irradiation that elevates system temperature above the thermal damage threshold of cell apoptosis and even leads to cell deconstruction.^{3–7} The specificity of nanoplatforms further permits us to direct cancer cell death without damaging healthy cells and tissues.^{8–10} Photothermal platforms are also applied as the carriers for drug loading and photocontrolled releasing.^{11,12} The combination of thermal therapy and targeted drug delivery is considered to optimize the effectiveness of photothermal therapy and conventional drug treatment.^{13–15} In addition, the development of photothermal platforms can compensate the lack of other emerging therapeutics. For instance, photodynamic therapy on the basis of the release of reactive oxygen species from light-active photosensitizers is a competitive candidate for cancer treat-

ment.^{16,17} But the inadequate selectivity, poor water-solubility, and in particular, intractable reactive oxygen production of most photosensitizers still limit the treatment of solid tumors. These disadvantages can be facily overcome by constructing photosensitizer-loaded photothermal nanoplatforms.^{18–21}

The capability to adsorb NIR irradiation between 700 and 1100 nm is the key for photothermal platforms, because skin and tissue exhibit minimal absorbance of light in this region and undergo minimum damage.^{7,8,22} Consequently, the nanoplatforms should be constructed from the materials with strong extinction and photothermal transduction behavior in the NIR region.^{23–26} The potential photothermal materials include organic compounds,²⁷ inorganic materials,^{7,25,28,29} carbon materials,^{30–32} and polymers,^{33–37} which have their own advantages and disadvantages. Upon irradiation, the organic compounds and polymers may suffer from photobleaching.^{38–40} Carbon materials possess a low molar extinction coefficient.³¹ Despite the high molar extinction coefficient and

Received: June 17, 2014

Accepted: August 9, 2014

Published: August 9, 2014

good photostability, the biocompatibility of inorganic materials is usually worse than that of organic materials.³³ As a result, photothermal nanoplateforms have been constructed by hybridization of the aforementioned photothermal materials to avoid the disadvantages. The composite structures of polymer-encapsulated inorganic nanoparticles (NPs) are ones of the mostly studied systems.²⁹ The inorganic NPs, typically noble metals and copper chalcogenides, mainly contribute to the photothermal performance, while the polymer envelopment makes the composites biocompatible.⁴¹

One of the key issues of practical photothermal nanoplateforms is the biodegradability. Although many inorganic NPs possess excellent photothermal performance, they are not biodegradable and remain in the body for a long time after treatment.⁴² For example, Au NPs are slowly excreted by liver and kidney.⁴³ The degradation rate of CuS NPs is faster than that of Au, but 10% CuS still remains in the body after 1 month of degradation.⁴³ The clinical photothermal platforms require a new class of biodegradable inorganic NPs. Fe₃O₄ NPs have been approved as safe nanomaterials in clinical applications, which are widely applied as the agents in magnetic resonance imaging (MRI), magnetically guided drug deliver and cell separation, hyperthermia treatment, and so forth.^{44,45} Fe₃O₄ is excreted mainly by feces, thus indicating low damage to organisms.^{46,47} Most recently, Fe₃O₄-polypyrrole (PPy) core/shell NPs have been fabricated and tested as low toxic, biodegradable, and multifunctional photothermal platforms (drug delivery and release, magnetic separation, MRI, and photothermal therapy).^{48–50} However, due to the low molar extinction coefficient and subsequent poor photothermal performance, the Fe₃O₄ core only contributes to the magnetism. The photothermal contribution is limited to the PPy shell.

Note that the organization of NPs into regular structures is an effective pathway for performance improvement. The directing of NP self-assembly into chainlike structures, hollow vesicles, or solid superparticles can significantly enhance the photothermal performance, owing to the optimization of NP electronic structures.^{51–55} It is reasonably expected to enhance the photothermal contribution of Fe₃O₄ by optimizing the spatial organization of Fe₃O₄ NPs in the composite nanoplateforms. In this paper, we demonstrate the development of composite photothermal platforms by combining the self-assembly of Fe₃O₄ NPs into spherical superstructures and the subsequent PPy envelopment. Leading from the optimized electronic structures, this system greatly increases the molar extinction coefficient of Fe₃O₄ NPs 300-fold and therewith improves the photothermal performance.

2. EXPERIMENTAL SECTION

2.1. Materials. Iron acetylacetonate (Fe(acac)₃, 99.9+%), 1,2-hexadecanediol (90%), benzyl ether (99%), oleyamine (OLA, 70%), oleic acid (OA, 90%), sodium dodecyl sulfate (SDS, 99%), poly(vinyl alcohol) (PVA, *M_w*: 13 000–23 000, 98%), phosphate buffered saline (PBS, dissolve 1 tablet in 200 mL of water, pH = 7.4) were purchased from Sigma-Aldrich. Pyrrole (Py, 99%) was purchased from Acros Organics. Dulbecco's modified Eagle's medium with high glucose (DMEM(H)) and fetal bovine serum (FBS) were purchased from Gibco. Propidium iodide (PI) was purchased from Invitrogen. Toluene, chloroform, and FeCl₃·6H₂O were analytical grade and used as received. Absolute ethanol and deionized water were used in all experiments.

2.2. Synthesis of Fe₃O₄ NPs. OA-stabilized Fe₃O₄ NPs were synthesized following a thermal decomposition method according to the previous publication.⁵⁶ Typically, 2 mmol Fe(acac)₃, 10 mmol 1,2-

hexadecanediol, 6 mmol OA, and 6 mmol OLA were mixed in 20 mL of benzyl ether. After the mixture was stirred for 15 min under nitrogen atmosphere, it was heated to 200 °C and maintained for 30 min, and then refluxed for another 30 min under 265 °C. After the solution cooled down to room temperature, it was treated with ethanol. The OA-stabilized Fe₃O₄ NPs were separated with the help of a magnet and dissolved in chloroform.

2.3. Preparation of Fe₃O₄ Superstructures. SDS-capped Fe₃O₄ superstructures were prepared by a microemulsion template technique following the method of our previously reported work.⁵⁷ The experiment started at room temperature, under a mechanical stirring and ultrasonic treatment, 0.2, 0.4, 0.6, and 1.0 mL Fe₃O₄ NP toluene solutions (10 mg/mL) were added dropwise into SDS aqueous solution (28 mg/mL, 5 mL) to form an oil-in-water microemulsion. By evaporating toluene at 55 °C, SDS-capped Fe₃O₄ superstructures with different diameters were prepared.

2.4. PPy-Capped Fe₃O₄ Superstructures. Five milliliter SDS-capped Fe₃O₄ superstructures with the diameter of 44.8 nm were collected by centrifugation and redispersed in 5 mL of deionized water. Subsequently, a specific amount of Py monomer, such as 1, 3, 5, and 10 μ L, was mixed with the Fe₃O₄ superstructure suspension. After the mixtures were stirred for 30 min, the mixtures were added dropwise into 20 mL of 12 mg/mL PVA aqueous solution containing 40 mg of FeCl₃·6H₂O under mechanical stirring. The color gradually turned black, showing the polymerization of Py. Twenty-four hours later, PPy-capped Fe₃O₄ superstructures were prepared.

2.5. Photothermal Tests. A 2 mL aqueous suspension of SDS- or PPy-capped Fe₃O₄ superstructures was injected in 1 × 1 × 4 cm quartz cuvette cell. A NIR diode laser (808 and 980 nm, LEO photonics Co. Ltd.) was delivered through the solution with specific power density and duration. The temperature variation was measured by thermometer (Fisher Scientific 14-648-12) at an interval of 30 s.

2.6. Cytotoxicity Assay. The human cervical carcinoma cell line (Hela cells) from Chinese Academy of Sciences Cell Bank (Shanghai, P. R. China) was cultured in DMEM(H) supplemented 10% FBS in a 5% CO₂ humidified atmosphere at 37 °C. In the assay, Hela cells were seeded on 96-well plates with a density of 3000 cells per well and incubated overnight. After the culture medium was discarded, the cells were incubated in 200 μ L DMEM(H) with 10% FBS and different concentrations of PPy-capped Fe₃O₄ superstructures at 37 °C for 24 h. The plates were analyzed for cell viability by standard methyl thiazolyl tetrazolium (MTT) assay. Each sample was assayed in 3 wells and repeated three times.

2.7. Photothermal Killing Hela Cells and Apoptosis Staining. Hela cells were seeded on 96-well plates with a density of 3000 cells per well and incubated overnight. After the culture medium was discarded, the cells were incubated in 200 μ L of DMEM(H) with 10% FBS and specific concentrations of PPy-capped Fe₃O₄ superstructures at 37 °C for 24 h. The samples were irradiated by an 808 nm NIR laser with different power densities for 10 min. The plates were analyzed for cell viability by MTT assay. Each laser power density was assayed in 3 wells and repeated three times. In the apoptosis staining experiment, Hela cells were seeded 30 000 cells per well on 6-well plates and incubated overnight. After the cells were rinsed for three times by PBS solution, the cells in each well were incubated in 1000 μ L of DMEM(H) with 10% FBS and specific concentrations of PPy-capped Fe₃O₄ superstructures at 37 °C for 4 h. Each sample was irradiated by an 808 nm NIR laser with different power densities for 10 min. Finally, the Hela cells were stained by 0.001 mg/mL PI.

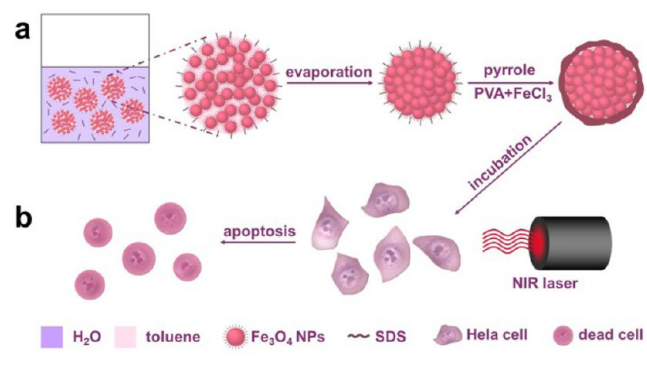
2.8. Characterization. Transmission electron microscopy (TEM) was operated using a Hitachi H-800 electron microscope at an acceleration voltage of 200 kV with a CCD camera. UV–vis absorption spectra were measured with a Shimadzu 3600 UV–vis–near-IR spectrophotometer. Dynamic light scattering (DLS) measurements were operated with a Zetasizer NanoZS (Malvern Instruments). Magnetic measurements were performed using a SQUID magnetometer (QD MPMS) at 300 K by cycling the magnetic field between –30 and +30 kOe. Thermogravimetric analysis (TGA) was measured on an American TA Q500 analyzer under N₂ atmosphere with the flow

rate of 100 mL/min. Bright field and fluorescent images of HeLa cells were obtained by an Olympus IX71 inverted fluorescence microscope.

3. RESULTS AND DISCUSSION

3.1. Self-Assembled Fe₃O₄ NP Superstructures with Improved Molar Extinction Coefficient. In our work, OA-stabilized Fe₃O₄ NPs are synthesized following a precursor thermal decomposition method according to the previous publication,⁵⁶ which produces the NPs with average diameter of 5.3 nm (Figure S1a, Supporting Information). Owing to the capping ligand of hydrophobic OA, the Fe₃O₄ NPs are dispersible in nonpolar solvents, such as toluene. Fe₃O₄ NP superstructures are fabricated according to a microemulsion template route, which employs the oil droplets in oil-in-water (O/W) microemulsion as the templates (Scheme 1a).^{57–59}

Scheme 1. Schematic Illustration of the Formation of PPY-Enveloped Fe₃O₄ NP Superstructures (a) and the Photothermal Killing HeLa Cells (b)



Typically, 1.0 mL of toluene solution of Fe₃O₄ NPs with the concentration of 10 mg/mL is added into 5 mL of 28 mg/mL SDS aqueous solution under ultrasonic treatment and mechanical stirring to form a microemulsion. After evaporation of toluene at 55 °C, SDS-capped Fe₃O₄ superstructures are fabricated by virtue of the hydrophobic–hydrophobic interaction in between OA-stabilized NPs and/or the alkyl chains of SDS. Resulting from the hydrophilic head of SDS, the as-prepared superstructures are dispersible in water. Under TEM, the superstructures appear as spheres with an average diameter of 63.9 nm and a deviation less than 5.5% (Figure 1a–c). DLS measurement indicates that the average diameter of Fe₃O₄ superstructures in the solution is 67.0 nm (Figure 1d). The DLS result is slightly bigger than that of TEM, because TEM only exhibits the size of dried structures. The magnetic curve of the superstructures is measured by cycling the magnetic field between –30 kOe and +30 kOe. As shown in Figure 1e, the saturation magnetization of the Fe₃O₄ superstructures is 60.5 emu/g, exhibiting the strong magnetism. The M(H) hysteresis curve is completely reversible, which means that the superstructures are superparamagnetic. This is the prerequisite for the application as MRI contrast media.⁴⁴ Due to the high saturation magnetization, the Fe₃O₄ superstructures can be separated from the suspension with the help of a magnet (Figure 1f). In comparison, the original Fe₃O₄ NPs are also superparamagnetic and exhibit the saturation magnetization of 61.6 emu/g (Figure S1b, Supporting Information). It reveals that the self-assembly process has little effect on the structures and hence the magnetism of Fe₃O₄ NPs.

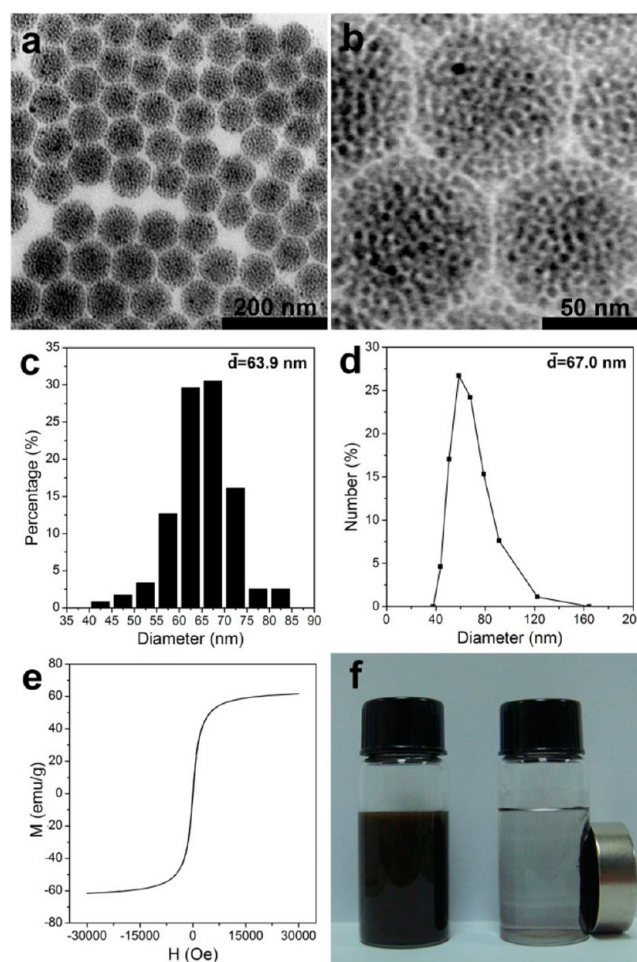


Figure 1. TEM images (a, b) and size distribution (c), DLS size distribution (d), and M-H curve (e) of SDS-capped Fe₃O₄ NP superstructures. (f) Photograph of the suspension of SDS-capped Fe₃O₄ superstructures without and with a magnet.

As shown in Figure S1c (Supporting Information), the molar extinction coefficient of Fe₃O₄ NPs is rather low, which is only around $3.65 \times 10^6 \text{ M}^{-1} \text{ cm}^{-1}$ at 808 nm. The lower molar extinction coefficient in comparison to that of gold and copper chalcogenide nanomaterials sheds the doubt of Fe₃O₄ NPs as efficient photothermal materials. Because the molar extinction coefficient of a given material should increase with material size, the self-assembly superstructures of Fe₃O₄ NPs are expected to exhibit a size-related increase of the molar extinction coefficient. In our experiment, the diameter of SDS-capped superstructures is tunable by altering the toluene-to-water ratio in the microemulsion, while the concentration of Fe₃O₄ toluene solution is fixed. As other experimental variables are fixed, the increase of the dose of Fe₃O₄ NP toluene solution from 0.2, 0.4, to 0.6 mL leads to the increase of the average diameter of Fe₃O₄ superstructures from 31.8, 44.8, to 50.1 nm (Figure 2). The size distribution of the superstructures stays narrow (Figure 2b,e,h). The true diameter of Fe₃O₄ superstructures in solution is revealed by DLS measurement, which is 37.7, 49.5, and 61.7 nm under the situation of increased Fe₃O₄ dose (Figure 2c,f,i). The DLS results are basically consistent with the TEM observation but slightly higher, because TEM results are the size of dried superstructures. Figure 3a indicates the extinction spectra of SDS-capped Fe₃O₄ superstructures with different size. With the increase of diameters, the extinction of

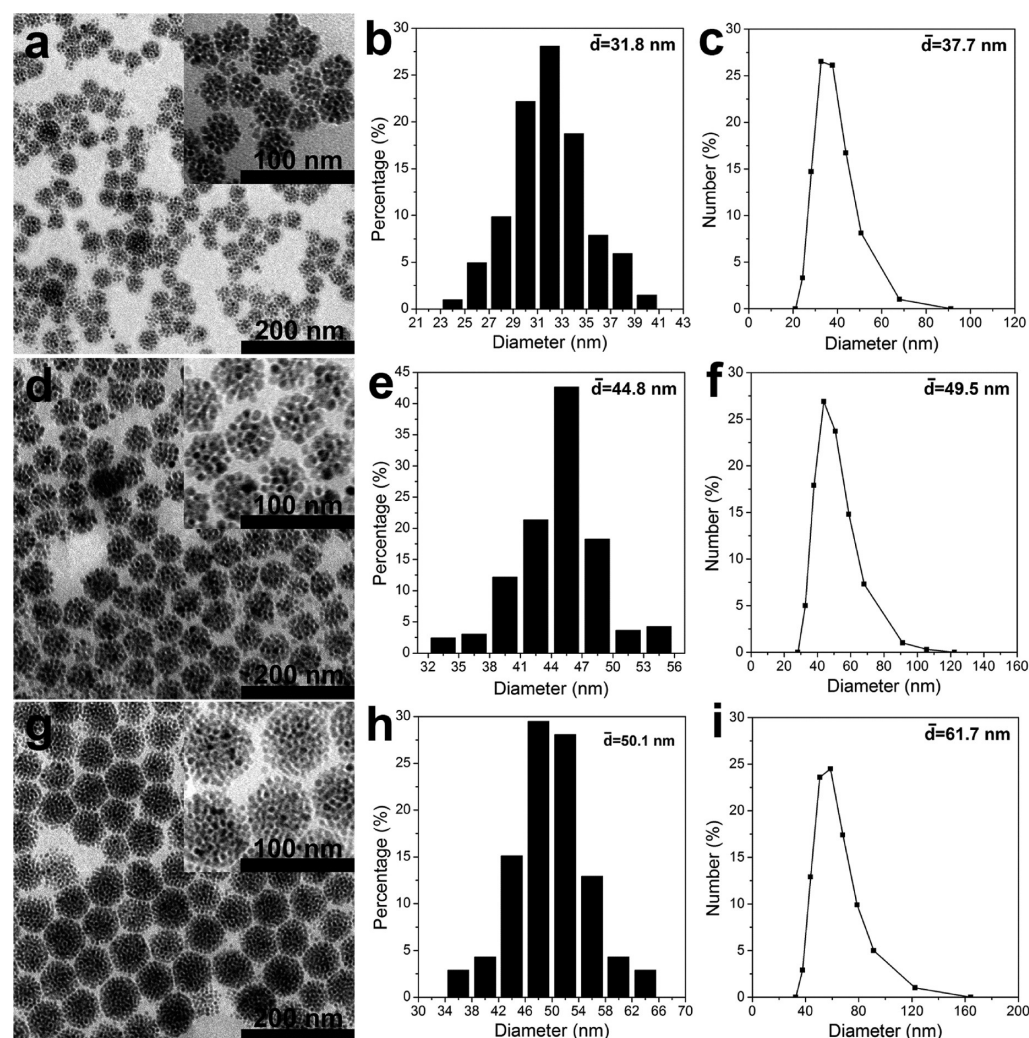


Figure 2. TEM images (a, d, g), size distribution (b, e, h), and DLS size distribution (c, f, i) of SDS-capped Fe_3O_4 superstructures with different diameters.

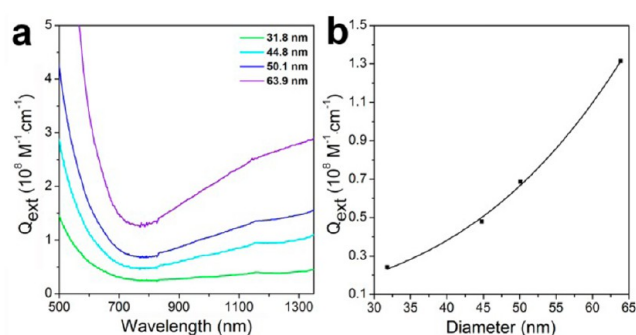


Figure 3. (a) Extinction spectra of SDS-capped Fe_3O_4 superstructures with the average diameters of 31.8, 44.8, 50.1, and 63.9 nm. (b) Extinction coefficient of SDS-capped Fe_3O_4 superstructures at 808 nm vs the diameters.

Fe_3O_4 superstructures in NIR region obviously increases. For the superstructures with the diameter of 63.9 nm, the molar extinction coefficient at 808 nm is $1.31 \times 10^8 \text{ M}^{-1} \text{ cm}^{-1}$, which is improved by 2 orders of magnitude in comparison to the original Fe_3O_4 NPs (Figure S1c, Supporting Information). The relation between the molar extinction coefficient and the diameter of Fe_3O_4 superstructures can be fitted with the curve

of $Q_{\text{ext}} = 0.0844 \times \exp(D/22.6) - 0.109$ (Figure 3b), where Q_{ext} is the molar extinction coefficient at 808 nm and D is the diameter of superstructures. This curve clearly reveals the rapid increase of molar extinction coefficient with the increase of superstructure diameters. The enhanced extinction in the NIR region is attributed to the optimization of the Fe_3O_4 electronic structure in the self-assembly architectures. Two types of electronic transitions may contribute to the extinction of Fe_3O_4 . Namely, Fe(III) ligand field transitions ($d-d$ transitions), and interactions between magnetically coupled Fe(III) ions.⁶⁰ In the current system, the extinction at NIR region is attributed to the indirect band gap transition of Fe(III) 3d electrons in Fe_3O_4 . For small Fe_3O_4 NPs, some sub-bands of the indirect transition are forbidden, resulting in the weak extinction at the NIR region. In the self-assembled architectures, the transition of these sub-bands is allowed by Brillouin zone folding.⁶¹ The new electronic structures generate strong extinction at the NIR region. As a result, the molar extinction coefficient increases with the diameters of Fe_3O_4 superstructures. In addition, the closely attached Fe_3O_4 NPs may increase the magnetic coupling of Fe(III) ions, also contributing to the enhanced NIR extinction.

3.2. Photothermal Property of Fe_3O_4 Superstructures. The self-assembly of Fe_3O_4 NPs into superstructures greatly

improves the photothermal performance. As shown in Figure 4, the temperature increment of 2 mL aqueous suspension of

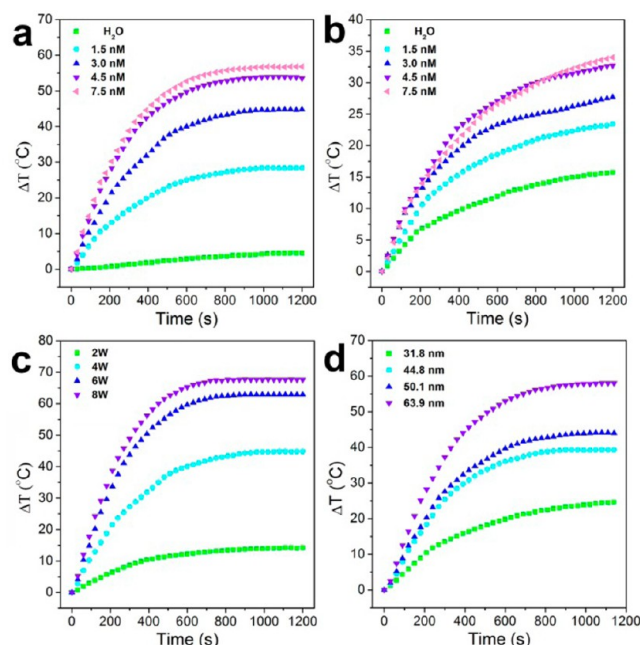


Figure 4. Temperature increment vs the concentration (a, b), power density (c), and size (d) of SDS-capped Fe_3O_4 NP superstructures. (a, b) 1.5, 3.0, 4.5, and 7.5 nM Fe_3O_4 superstructures, referring to the number of superstructures, with the average diameter of 63.9 nm are irradiated with 4 W/cm^2 808 nm laser (a) and 0.726 W/cm^2 980 nm laser (b). (c) 3 nM Fe_3O_4 superstructures with the average diameter of 63.9 nm are irradiated by 808 nm laser with different power density. (d) 7.5 nM Fe_3O_4 superstructures with different diameters are irradiated by 4 W/cm^2 808 nm laser. The initial temperature is 23 $^{\circ}\text{C}$.

SDS-capped Fe_3O_4 superstructure is studied by irradiating the suspension using a NIR laser. With the increase of superstructure concentration, an obvious temperature increment is found both for the irradiation with an 808 and 980 nm laser (Figure 4a,b). The irradiation of 1.5 nM Fe_3O_4 superstructures using an 808 nm laser for 10 min leads to the temperature

increment of 25.0 $^{\circ}\text{C}$, whereas the temperature increment is 52.7 $^{\circ}\text{C}$ as the concentration is increased to 7.5 nM. This is attributed to the collective heating effect of the suspension with high superstructure concentration.^{54,55} More irradiation is absorbed by the suspension with high Fe_3O_4 concentration and converted into heat energy. In addition, the increased power density of laser also makes the temperature increment more obvious (Figure 4c), because high dose of irradiation is imposed into the suspension. Most importantly, the Fe_3O_4 superstructures with larger sizes lead to more obvious temperature increments (Figure 4d). To exclude the influence of Fe_3O_4 quality, the photothermal property is studied by fixing the total quality of Fe_3O_4 but altering the diameters of the superstructures (Figure S2, Supporting Information). With the same mass concentration of Fe_3O_4 , bigger superstructures exhibit more obvious temperature increments than the smaller ones, though the concentration is lowered. For instance, the temperature increment of the superstructures with the diameter of 63.9 nm is 24.3 $^{\circ}\text{C}$, which is 5.8 $^{\circ}\text{C}$ higher than that of the 31.8 nm superstructures. Because the power density, irradiation duration, and the quality of Fe_3O_4 are fixed, this result undoubtedly confirms that the formation of self-assembly architectures is capable to improve the photothermal performance.

Two parameters may contribute to the photothermal performance. One is photothermal transduction efficiency (η). The other is the molar extinction coefficient. The η of both Fe_3O_4 superstructures and the original NPs are calculated and compared according to the previous report (Figures S3 and S4, Supporting Information).⁶² The η of the self-assembled superstructures and the unassembled NPs is 54.5% and 75.9%, respectively. In addition, with the increase of superstructure diameter from 31.8, 44.8 to 50.1 nm, η decreases from 65.9, 58.0 to 56.6%. It means that larger Fe_3O_4 nanostructures possess lower η , because of the stronger Rayleigh scattering. These results reveal that η is not the reason for the improved photothermal performance in our system. Note that η only means the capability of energy conversion through photothermal pathway rather than the absolute photothermal performance of the materials. In the current system, the molar extinction coefficient of Fe_3O_4 is improved with 2 orders

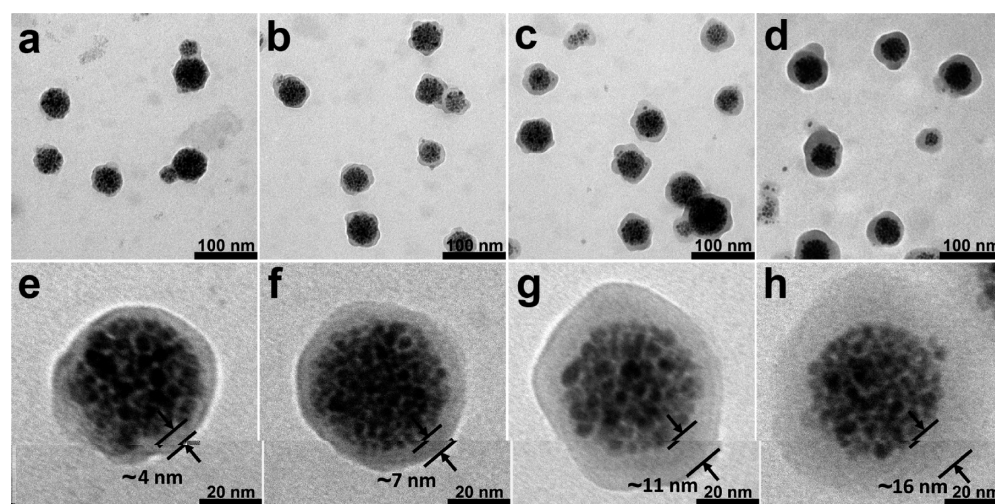


Figure 5. TEM images of PPy-capped Fe_3O_4 superstructures with the PPy thickness of 4, 7, 11, and 16 nm that are prepared with the addition of 1 (a, e), 3 (b, f), 5 (c, g), and 10 μL (d, h) pyrrole monomer into the reaction system.

of magnitude by forming self-assembled architectures, which greatly increases the capability to absorb light. Whereas, η only decreases slightly. So, more laser irradiation is employed by Fe_3O_4 superstructures for generating heat, thus leading to the improved photothermal performance. This consideration is supported by the experimental results that the shape of the ΔT -to-diameter curve is much similar to that of the Q_{ext} -to-diameter curve (Figures 3b and S2, Supporting Information).

3.3. PPy-Capped Fe_3O_4 Superstructures. To improve the stability and photothermal performance, the self-assembled Fe_3O_4 superstructures are further enveloped with a PPy shell to form PPy-capped Fe_3O_4 superstructures. Despite the 63.9 nm superstructures possess the best photothermal performance, their diameter is also the biggest. The diameter will further increase to around 100 nm after PPy capping. The bigger superstructures will greatly affect cellular uptake. So, in the current study, the 44.8 nm superstructures are used to prepare the PPy-capped superstructures. In the experiment, pyrrole monomers directly polymerize on the surface of superstructures through oxidation polymerization. The surface of SDS-capped superstructures is negative owing to the negatively charged SDS. Pyrrole possesses positive charges. Consequently, pyrrole greatly tends to adsorb on the surface of superstructures through electrostatic attraction. After the suspension is mixed with FeCl_3 , it gradually turns black, implying the polymerization of pyrrole. Note that the adsorption of positive Fe^{3+} on SDS-capped superstructures is also favored by electrostatic attraction, and the oxidation polymerization is mediated by Fe^{3+} . So, the polymerization of pyrrole on superstructure surface is favorable. A clear core/shell structure is observed by TEM observation after polymerization (Figure 5). The dark part in the center of observed spheres is assigned to inorganic Fe_3O_4 , whereas the light shell is assigned to PPy. The shell thickness is tunable by altering the concentration of pyrrole monomers. As the dose of pyrrole monomers is increased from 1, 3, 5 to 10 μL , the thickness of PPy shell increases from around 4, 7, 11 to 16 nm. TGA shows the increase of organic content from 4.9, 6.6, 11.0 to 15.9% (Figure S5, Supporting Information), consistent with the TEM-observed thickness increase of the PPy shell.

In the absence of the PPy shell, Fe_3O_4 superstructures completely precipitate after 18 h of storage in PBS. Although the stability of Fe_3O_4 superstructures in water, FBS, and DMEM(H) is better than in PBS, obvious sediment is found after 3 weeks of storage (Figure S6a, Supporting Information). In contrast, the colloidal and physiological stability are improved after PPy enveloping. PPy-capped superstructures are very stable in water and PBS after 3 weeks of storage. As stored in FBS and DMEM(H), trace amounts of precipitation are observed after 66 h of storage, but do not increase during the prolonged storage (Figure S6b, Supporting Information).

The formation of the PPy shell further enhances the molar extinction coefficient of Fe_3O_4 -based materials. As indicated in Figure 6a, the molar extinction coefficient of the composite superstructures at 808 nm is increased to $1.12 \times 10^9 \text{ M}^{-1}\cdot\text{cm}^{-1}$, which is 1 order of magnitude higher than that of SDS-capped Fe_3O_4 superstructures. In addition, the molar extinction coefficient increases with the thickness increment of PPy shell (Figure 6b), confirming the contribution of the PPy shell on the extinction. It is known that the extinction intensity is associated with the available electrons in the oscillation system.^{1,8} As a conductive polymer, PPy can provide additional electrons oscillating. With the increase of PPy thickness, more

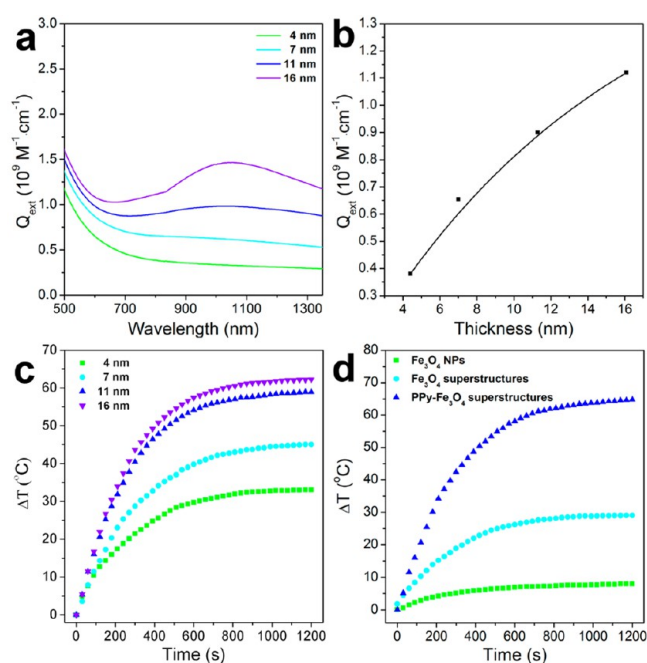


Figure 6. (a) Extinction spectra of PPy-capped Fe_3O_4 superstructures with different thickness of PPy shell. (b) Extinction coefficient of PPy-capped Fe_3O_4 superstructures at 808 nm vs the thickness of PPy shell. (c) Temperature increment of 1 nM PPy-capped Fe_3O_4 superstructure suspensions with different PPy thickness. The suspensions are irradiated by an 808 nm laser with a power density of 4 W/cm^2 . (d) Temperature increment of 3 nM SDS-capped Fe_3O_4 NPs, SDS-capped Fe_3O_4 superstructure, and PPy-capped Fe_3O_4 superstructure. The power density is 4 W/cm^2 . The thickness of the PPy shell is 4 nm.

electrons are supplied in the composite superstructures, and therefore the continuous increase of the extinction intensity. The improved molar extinction coefficient means that the composite superstructures should possess a stronger ability in harvesting NIR irradiation, thus exhibiting better photothermal performance. The molar extinction coefficient and the thickness of the PPy shell fit with the curve of $Q_{\text{ext}} = -1.79 \times \exp(H/14.0) + 0.169$ (Figure 6b), where H is the thickness of the PPy shell. This curve clearly indicates that although PPy shell contributes to the extinction coefficient, the influence becomes less obvious with the increase of shell thickness. The result is well consistent with that of the previous studies of PPy-capped Au photothermal agents.⁵¹

The photothermal performance of PPy-capped Fe_3O_4 superstructures is revealed by measuring the temperature increment of 2 mL 1 nM composite superstructures using 808 nm laser irradiation with a power density of 4 W/cm^2 (Figure 6c). As the thickness of the PPy shell increases from 4 to 11 nm, the system exhibits more obvious temperature increments, which corresponds with the increase of the molar extinction coefficient. However, further increase of the thickness to 16 nm does not lead to obvious temperature increments (Figure S7, Supporting Information). This mainly attributes to the stronger light scattering of bigger structures.⁵¹ It is known that as the diameter of NPs exceeds 50 nm, the light scattering will rapidly increase with size increments. As the thickness of PPy increases from 11 to 16 nm, the diameter of superstructures increases from 67 to 77 nm. So, although the 16 nm one possesses the highest extinction coefficient (Figure 6b), the strong light scattering makes the temperature increment not so obvious. This result also reveals that a thin layer of PPy

shell of about 12 nm is enough, while further increase of PPy thickness is unnecessary. For a clear comparison, the temperature increment of SDS-capped Fe_3O_4 NPs, SDS-capped Fe_3O_4 superstructures, and PPy-capped superstructures under 808 nm laser irradiation are shown in Figure 6d. Obviously, at the same mass concentration, the temperature increment of PPy-capped superstructures is much higher than that of the SDS-capped superstructures and then Fe_3O_4 NPs. As mentioned above, the different magnitudes of temperature increments are mainly attributed to the increased molar extinction coefficient of PPy-capped superstructures, thus optimizing the Fe_3O_4 electronic structure and hence the light harvest upon NIR irradiation.

The η of PPy-capped superstructures is calculated to be 49.0% with the PPy shell of 16 nm, in between the η of pure PPy NPs and the superstructures without PPy shell (Figures S4 and S8, Supporting Information). As for the composite superstructures with a PPy shell of 4, 7, and 11 nm, the η is 48.7, 48.9, and 47.4% without obvious differences. These results confirm that besides the size of nanostructures, the η is mainly determined by the species of materials. As reported by the previous publications, the η of several photothermal materials of PPy NPs, Cu_2S NPs, and Au nanorods is 44.7,³⁵ 25.7,⁶³ and 21%,⁶⁴ respectively. This means that the PPy-capped Fe_3O_4 superstructures can effectively convert the absorbed light into heat energy, which is comparable with the most studied photothermal materials.

3.4. In Vitro Photothermal Therapy. Hela cells are selected to investigate the photothermal effect of PPy-capped Fe_3O_4 superstructures. The toxicity of composite superstructures is studied by standard MTT assay. Hela cells are incubated in the culture media in the presence of PPy-capped Fe_3O_4 superstructures with different concentrations for 24 h. As displayed in Figure 7, the viabilities of Hela cells are more than

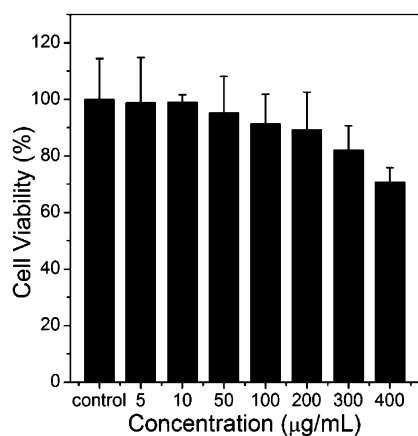


Figure 7. Cytotoxicity of PPy-capped Fe_3O_4 superstructures, which is tested by incubating Hela cells in 200 μL culture medium with different concentrations of the superstructures for 24 h, and followed by MTT assay. Data are shown as the means \pm standard error of the means. 100 $\mu\text{g}/\text{mL}$ corresponds to 0.11 nM.

90% below the concentration of 0.11 nM. Even when the concentration is increased to 0.46 nM, the viability is still 73%. This reveals the low cell toxicity of PPy-capped Fe_3O_4 superstructures. The slight toxicity is attributed to the remaining SDS on the superstructures, whereas the PPy shell is almost nontoxic.⁴⁸ To further lower the toxicity, polyethylene

glycol-contained amphiphilic polymers can be coated on the superstructures.⁴⁹

The *in vitro* photothermal therapy is tested by NIR irradiating Hela cells that are foremost incubated with PPy-capped Fe_3O_4 superstructures (Figure 8). The thickness of PPy is 11 nm. After NIR laser treatment, the cells are stained with PI, which penetrates dead cells only.^{4,33} As shown in Figure 8a–c, the ratio of red cells increases with the increase of laser intensity, representing the accelerated cell death under stronger NIR irradiation. Both the fluorescent and bright field images indicate the volume reduction of Hela cells (Figure 8a–f), which means cell apoptosis. In comparison, the NIR irradiation of Hela cells incubated without Fe_3O_4 superstructures does not lead to cell volume variation (Figure S9, Supporting Information). In addition, almost no cells are stained by PI. This means that sole NIR irradiation has no effect on cell apoptosis, thus confirming the role of Fe_3O_4 superstructures as an effective photothermal platform. The cell viability after laser treatment is exhibited by MTT assay. As the power density of the 808 nm laser reaches 1 W/cm^2 , the viability of the Hela cells in the presence of Fe_3O_4 superstructures is less than 20% (Figure 8g). The cell viability further decreases to 5%, when the power density is increased to 1.5 W/cm^2 . In contrast, the 808 nm irradiation does not decrease the viability of Hela cells obviously in the absence of Fe_3O_4 superstructures. PPy-capped Fe_3O_4 superstructures with the PPy thickness of 16 nm are also studied (Figure S10, Supporting Information). Their photothermal effect is slightly worse than that of the 11 nm one, which confirms the aforementioned consideration that a thin layer of a PPy shell of about 12 nm is enough. Figure 8h indicates the influence of Fe_3O_4 superstructure concentration on photothermal therapy. The cell viability decreases with the increase of superstructure concentration. As the concentration reaches 0.057 nM, the cell viability is 20%. The increase of superstructure concentration over 0.068 nM further decreases the viability below 10%. PI staining experiment also proves that Hela cells are killed by virtue of the photothermal behavior of Fe_3O_4 superstructures (Figure S11, Supporting Information). These results confirm that the photothermal behavior of PPy-capped Fe_3O_4 superstructures is capable to lead the apoptosis of Hela cells. It should be mentioned that the apoptosis temperature of ordinary cells is generally 1–2 $^{\circ}\text{C}$ higher than cancer cells. This means that the current method is more effective for photothermal ablation of cancer cells.

Finally, by inheriting the strong superparamagnetism of Fe_3O_4 , PPy-capped Fe_3O_4 superstructures exhibit a concentration-dependent darkening effect in T2-weighted MR imaging (Figure S12, Supporting Information). This confirms the application of PPy-capped Fe_3O_4 superstructures as MRI contrast media.

4. CONCLUSIONS

In summary, monodisperse Fe_3O_4 spherical superstructures with controlled diameters are prepared from the as-prepared Fe_3O_4 NPs using the oil droplets in O/W microemulsion as the templates. In comparison with the unassembled NPs, the self-assembled superstructures exhibit size-dependent and remarkably enhanced molar extinction coefficients in the NIR region up to 2 orders of magnitude. To improve the stability and photothermal performance, the Fe_3O_4 superstructures are enveloped with a PPy shell via oxidative polymerization. On the one hand, the PPy shell increases the colloidal and physiological stability of Fe_3O_4 superstructures. On the other

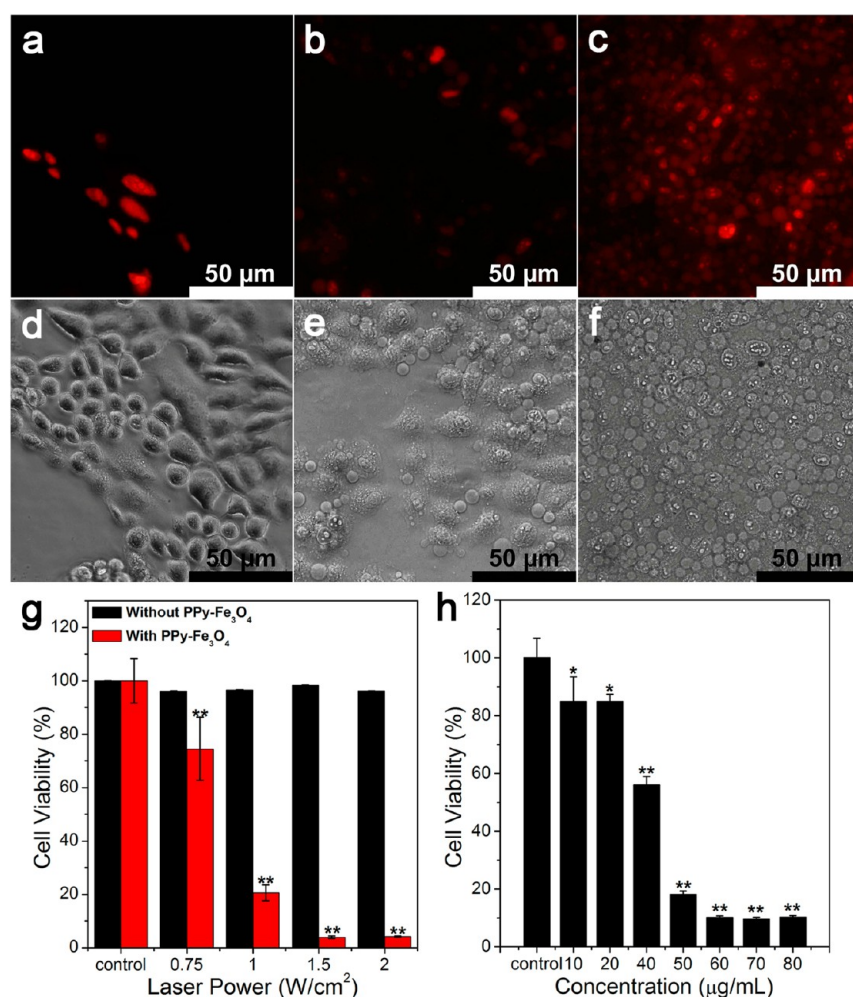


Figure 8. Fluorescent (a–c) and bright field (d–f) images of HeLa cells after irradiated by an 808 nm laser with the power density of 0.5 (a, d), 1 (b, e), and 1.5 (c, f) W/cm² for 10 min. (g) HeLa cell viabilities after 808 nm laser irradiation with the power density of 0.75, 1, 1.5, and 2 W/cm² for 10 min. The HeLa cells are foremost incubated with 80 μg/mL PPy-capped Fe₃O₄ superstructures for 4 h. The thickness of PPy shell is 11 nm. (h) HeLa cell viabilities versus the concentration of PPy-capped Fe₃O₄ superstructures, which is studied by 808 nm laser irradiation with the power density of 1.5 W/cm² for 10 min. Data are shown as the means ± standard error of the means, * $p < 0.05$ and ** $p < 0.01$. 100 μg/mL corresponds to 0.11 nM.

hand, the molar extinction coefficient is further improved by 1 order of magnitude. The photothermal transduction efficiency of Fe₃O₄ superstructures and composite superstructures is calculated to be 54.5 and 49.0%, respectively, which is among the materials with the highest photothermal transduction efficiency. The PPy-capped Fe₃O₄ superstructures exhibit good photothermal performance, represented by the rapid temperature increments upon NIR laser irradiation. Primary cell tests indicate that the composite superstructures possess low toxicity and are effective for photothermal killing HeLa cells. Because PPy-capped Fe₃O₄ superstructures are multifunctional, less expensive, biocompatible, and biodegradable, they will be promising photothermal nanoplateforms for developing novel diagnostic and therapeutic techniques.

■ ASSOCIATED CONTENT

● Supporting Information

Additional TEM image, M-H curve, extinction spectrum, temperature increment, TGA curves, photographs, fluorescent and bright field images, cell viability, T2-weighted MR imaging, and method for calculating photothermal transduction efficiency. This material is available free of charge via the Internet at <http://pubs.acs.org>.

■ AUTHOR INFORMATION

Corresponding Authors

*H. Zhang. Fax: +86 431 85193423. Tel: +86 431 85159205. E-mail: hao_zhang@jlu.edu.cn.

*H. Sun. Fax: +86 431 85193423. Tel: +86 431 85159205. E-mail: hcsun@mail.jlu.edu.cn.

Notes

The authors declare no competing financial interest.

■ ACKNOWLEDGMENTS

This work was supported by NSFC (21374042, 21174051, 21221063, 81320108011), the 973 Program of China (2014CB643503), Natural Science Foundation of Jilin Province (201215030, 20140101048JC), the Special Project from MOST of China, and the Fundamental Research Funds for the Central Universities.

■ REFERENCES

(1) Zhang, Z. J.; Wang, J.; Chen, C. Y. Near-Infrared Light-Mediated Nanoplateforms for Cancer Thermo-Chemotherapy And Optical Imaging. *Adv. Mater.* **2013**, 25, 3869–3880.

- (2) Wu, W. T.; Shen, J.; Banerjee, P.; Zhou, S. Q. A Multifunctional Nanoplatfrom Based on Responsive Fluorescent Plasmonic ZnO-Au@PEG Hybrid Nanogels. *Adv. Funct. Mater.* **2011**, *21*, 2830–2839.
- (3) Maltzahn, G. V.; Park, J. H.; Agrawal, A.; Bandaru, N. K.; Das, S. K.; Sailor, M. J.; Bhatia, S. N. Computationally Guided Photothermal Tumor Therapy Using Long-Circulating Gold Nanorod Antennas. *Cancer Res.* **2009**, *69*, 3892–3900.
- (4) Melancon, M. P.; Zhou, M.; Li, C. Cancer Theranostics with Near-Infrared Light-Activatable Multimodal Nanoparticles. *Acc. Chem. Res.* **2011**, *44*, 947–956.
- (5) Huang, C. C.; Su, C. H.; Li, W. M.; Liu, T. Y.; Chen, J. H.; Yeh, C. S. Bifunctional Gd₂O₃/C Nanoshells for MR Imaging and NIR Therapeutic Applications. *Adv. Funct. Mater.* **2009**, *19*, 249–258.
- (6) Moon, H. K.; Lee, S. H.; Choi, H. C. *In Vivo* Near-Infrared Mediated Tumor Destruction by Photothermal Effect of Carbon Nanotubes. *ACS Nano* **2009**, *3*, 3707–3713.
- (7) Kennedy, L. C.; Bickford, L. R.; Lewinski, N. A.; Coughlin, A. J.; Hu, Y.; Day, E. S.; West, J. L.; Drezek, R. A. A New Era for Cancer Treatment: Gold-Nanoparticle-Mediated Thermal Therapies. *Small* **2011**, *7*, 169–183.
- (8) Jain, P. K.; Huang, X. H.; El-Sayed, I. H.; El-Sayed, M. A. Noble Metals on the Nanoscale: Optical and Photothermal Properties and Some Applications in Imaging, Sensing, Biology, and Medicine. *Acc. Chem. Res.* **2008**, *41*, 1578–1586.
- (9) Chen, J. Y.; Wang, D. L.; Xi, J. F.; Au, L.; Siekkinen, A.; Warsen, A.; Li, Z. Y.; Zhang, H.; Xia, Y. N.; Li, X. D. Immuno Gold Nanocages with Tailored Optical Properties for Targeted Photothermal Destruction of Cancer Cells. *Nano Lett.* **2007**, *7*, 1318–1322.
- (10) Qin, Z. P.; Bischof, J. C. Thermophysical and Biological Responses of Gold Nanoparticle Laser Heating. *Chem. Soc. Rev.* **2012**, *41*, 1191–1217.
- (11) You, J.; Zhang, G. D.; Li, C. Exceptionally High Payload of Doxorubicin in Hollow Gold Nanospheres for Near-Infrared Light-Triggered Drug Release. *ACS Nano* **2010**, *4*, 1033–1041.
- (12) Gui, R. J.; Wan, A. J.; Liu, X. F.; Jin, H. Intracellular Fluorescent Thermometry and Photothermal-Triggered Drug Release Developed from Gold Nanoclusters and Doxorubicin Dual-Loaded Liposomes. *Chem. Commun.* **2014**, *50*, 1546–1548.
- (13) Kim, J.; Lee, J. E.; Lee, S. H.; Yu, J. H.; Lee, J. H.; Park, T. G.; Hyeon, T. Designed Fabrication of a Multifunctional Polymer Nanomedical Platform for Simultaneous Cancer-Targeted Imaging and Magnetically Guided Drug Delivery. *Adv. Mater.* **2008**, *20*, 478–483.
- (14) Dong, K.; Liu, Z.; Li, Z. H.; Ren, J. S.; Qu, X. G. Hydrophobic Anticancer Drug Delivery by a 980 nm Laser-Driven Photothermal Vehicle for Efficient Synergistic Therapy of Cancer Cells in Vivo. *Adv. Mater.* **2013**, *25*, 4452–4458.
- (15) Zhang, W.; Guo, Z. Y.; Huang, D. Q.; Liu, Z. M.; Guo, X.; Zhong, H. Q. Synergistic Effect of Chemo-Photothermal Therapy Using PEGylated Graphene Oxide. *Biomaterials* **2011**, *32*, 8555–8561.
- (16) Huang, P.; Lin, J.; Wang, X. S.; Wang, Z.; Zhang, C. L.; He, M.; Wang, K.; Chen, F.; Li, Z. M.; Shen, G. X.; Cui, D. X.; Chen, X. Y. Light-Triggered Theranostics Based on Photosensitizer-Conjugated Carbon Dots for Simultaneous Enhanced-Fluorescence Imaging and Photodynamic Therapy. *Adv. Mater.* **2012**, *24*, 5104–5110.
- (17) Tian, J. W.; Ding, L.; Xu, H. J.; Shen, Z.; Ju, H. X.; Jia, L.; Bao, L.; Yu, J. S. Cell-Specific and pH-Activatable Rubryrin-Loaded Nanoparticles for Highly Selective Near-Infrared Photodynamic Therapy against Cancer. *J. Am. Chem. Soc.* **2013**, *135*, 18850–18858.
- (18) Lin, J.; Wang, S. J.; Huang, P.; Wang, Z.; Chen, S. H.; Niu, G.; Li, W. W.; He, J.; Cui, D. X.; Lu, G. M.; Chen, X. Y.; Nie, Z. H. Photosensitizer-Loaded Gold Vesicles with Strong Plasmonic Coupling Effect for Imaging-Guided Photothermal/Photodynamic Therapy. *ACS Nano* **2013**, *7*, 5320–5329.
- (19) Jang, B.; Park, J. Y.; Tung, C. H.; Kim, I. H.; Choi, Y. D. Gold Nanorod-Photosensitizer Complex for Near-Infrared Fluorescence Imaging and Photodynamic/Photothermal Therapy in Vivo. *ACS Nano* **2011**, *5*, 1086–1094.
- (20) Peng, J. J.; Zhao, L. Z.; Zhu, X. J.; Sun, Y.; Feng, W.; Gao, Y. H.; Wang, L. Y.; Li, F. Y. Hollow Silica Nanoparticles Loaded with Hydrophobic Phthalocyanine for Near-Infrared Photodynamic and Photothermal Combination Therapy. *Biomaterials* **2013**, *34*, 7905–7912.
- (21) Wang, J.; You, M. X.; Zhu, G. Z.; Shukoor, M. I.; Chen, Z.; Zhao, Z. L.; Altman, M. B.; Yuan, Q.; Zhu, Z.; Chen, Y.; Huang, C. Z.; Tan, W. H. Photosensitizer-Gold Nanorod Composite for Targeted Multimodal Therapy. *Small* **2013**, *9*, 3678–3684.
- (22) De, M.; Ghosh, P. S.; Rotello, V. M. Applications of Nanoparticles in Biology. *Adv. Mater.* **2008**, *20*, 4225–4241.
- (23) Chen, J. Y.; Wiley, B.; Li, Z. Y.; Campbell, D.; Saeki, F.; Cang, H.; Au, L.; Lee, J.; Li, X. D.; Xia, Y. N. Gold Nanocages: Engineering Their Structure for Biomedical Applications. *Adv. Mater.* **2005**, *17*, 2255–2261.
- (24) Zoric, I.; Zach, M.; Kasemo, B.; Langhammer, C. Gold, Platinum, and Aluminum Nanodisk Plasmons: Material Independence, Subradiance, and Damping Mechanisms. *ACS Nano* **2011**, *5*, 2535–2546.
- (25) Wang, Y. C.; Black, K. C. L.; Luehmann, H.; Li, W. Y.; Zhang, Y.; Cai, X.; Wan, D. H.; Liu, S. Y.; Li, M.; Kim, P.; Li, Z. Y.; Wang, L. H. V.; Liu, Y. J.; Xia, Y. N. Comparison Study of Gold Nanohexapods, Nanorods, and Nanocages for Photothermal Cancer Treatment. *ACS Nano* **2013**, *7*, 2068–2077.
- (26) Bu, X. Y.; Zhou, D.; Li, J.; Zhang, X.; Zhang, K.; Zhang, H.; Yang, B. Copper Sulfide Self-Assembly Architectures with Improved Photothermal Performance. *Langmuir* **2014**, *30*, 1416–1423.
- (27) Yang, J.; Choi, J.; Bang, D.; Kim, E.; Lim, E. K.; Park, H.; Suh, J. S.; Lee, K.; Yoo, K. H.; Kim, E. K.; Huh, Y. M.; Haam, S. Convertible Organic Nanoparticles for Near-Infrared Photothermal Ablation of Cancer Cells. *Angew. Chem., Int. Ed.* **2011**, *50*, 441–444.
- (28) Chen, Z. G.; Wang, Q.; Wang, H. L.; Zhang, L. S.; Song, G. S.; Song, L. L.; Hu, J. Q.; Wang, H. Z.; Liu, J. S.; Zhu, M. F.; Zhao, D. Y. Ultrathin PEGylated W₁₈O₄₉ Nanowires as a New 980 nm-Laser-Driven Photothermal Agent for Efficient Ablation of Cancer Cells in Vivo. *Adv. Mater.* **2013**, *25*, 2095–2100.
- (29) Xiao, Q. F.; Zheng, X. P.; Bu, W. B.; Ge, W. Q.; Zhang, S. J.; Chen, F.; Xing, H. Y.; Ren, Q. G.; Fan, W. P.; Zhao, K. L.; Hua, Y. Q.; Shi, J. L. A Core/Satellite Multifunctional Nanotheranostic for *in Vivo* Imaging and Tumor Eradication by Radiation/Photothermal Synergistic Therapy. *J. Am. Chem. Soc.* **2013**, *135*, 13041–13048.
- (30) Li, M.; Yang, X. J.; Ren, J. S.; Qu, K. G.; Qu, X. G. Using Graphene Oxide High Near-Infrared Absorbance for Photothermal Treatment of Alzheimer's Disease. *Adv. Mater.* **2012**, *24*, 1722–1728.
- (31) Kim, J. W.; Galanzha, E. I.; Shashkov, E. V.; Moon, H. M.; Zharov, V. P. Golden Carbon Nanotubes as Multimodal Photoacoustic and Photothermal High-Contrast Molecular Agents. *Nat. Nanotechnol.* **2009**, *231*, 688–694.
- (32) Antaris, A. L.; Robinson, J. T.; Yaghi, O. K.; Hong, G. S.; Diao, S.; Luong, R.; Dai, H. J. Ultra-Low Doses of Chirality Sorted (6,5) Carbon Nanotubes for Simultaneous Tumor Imaging and Photothermal Therapy. *ACS Nano* **2013**, *7*, 3644–3652.
- (33) Yang, K.; Xu, H.; Cheng, L.; Sun, C. Y.; Wang, J.; Liu, Z. *In Vitro* and *in Vivo* Near-Infrared Photothermal Therapy of Cancer Using Polypyrrole Organic Nanoparticles. *Adv. Mater.* **2012**, *24*, 5586–5592.
- (34) Zhu, Z. B.; Yue, X. L.; Ren, Q. S.; Dai, Z. F. Uniform Polypyrrole Nanoparticles with High Photothermal Conversion Efficiency for Photothermal Ablation of Cancer Cells. *Adv. Mater.* **2013**, *25*, 777–782.
- (35) Chen, M.; Fang, X. L.; Tang, S. H.; Zheng, N. F. Polypyrrole Nanoparticles for High-Performance *in Vivo* Near-Infrared Photothermal Cancer Therapy. *Chem. Commun.* **2012**, *48*, 8934–8936.
- (36) Zhou, J.; Lu, Z. G.; Zhu, X. J.; Wang, X. J.; Liao, Y.; Ma, Z. F.; Li, F. Y. NIR Photothermal Therapy Using Polyaniline Nanoparticles. *Biomaterials* **2013**, *34*, 9584–9592.
- (37) Lin, L. S.; Cong, Z. X.; Cao, J. B.; Ke, K. M.; Peng, Q. L.; Gao, J. H.; Yang, H. H.; Liu, G.; Chen, X. Y. Multifunctional Fe₃O₄@Polydopamine Core-Shell Nanocomposites for Intracellular mRNA

Detection and Imaging-Guided Photothermal Therapy. *ACS Nano* **2014**, *8*, 3876–3883.

(38) Kakiuchida, H.; Takahashi, M.; Tokuda, Y.; Yoko, T. Rewritable Holographic Structures Formed in Organic-Inorganic Hybrid Materials by Photothermal Processing. *Adv. Funct. Mater.* **2009**, *19*, 2569–2576.

(39) Skala, M. C.; Crow, M. J.; Wax, A.; Izatt, J. A. Photothermal Optical Coherence Tomography of Epidermal Growth Factor Receptor in Live Cells Using Immunotargeted Gold Nanospheres. *Nano Lett.* **2008**, *8*, 3461–3467.

(40) Cognet, L.; Tardin, C.; Boyer, D.; Choquet, D.; Tamarat, P.; Lounis, B. Single Metallic Nanoparticle Imaging for Protein Detection in Cells. *Proc. Natl. Acad. Sci. U. S. A.* **2003**, *100*, 11350–11355.

(41) Boca, S. C.; Potara, M.; Gabudean, A. M.; Juhem, A.; Baldeck, P. L.; Astilean, S. Chitosan-Coated Triangular Silver Nanoparticles as a Novel Class of Biocompatible, Highly Effective Photothermal Transducers for *in Vitro* Cancer Cell Therapy. *Cancer Lett.* **2011**, *311*, 131–140.

(42) Sharifi, S.; Behzadi, S.; Laurent, S.; Forrest, M. L.; Stroeve, P.; Mahmoudi, M. Toxicity of Nanomaterials. *Chem. Soc. Rev.* **2012**, *41*, 2323–2343.

(43) Guo, L.; Panderi, I.; Yan, D. D.; Szulak, K.; Li, Y. J.; Chen, Y. T.; Ma, H.; Niesen, D. B.; Seeram, N.; Ahmed, A.; Yan, B. F.; Pantazatos, D.; Lu, W. A Comparative Study of Hollow Copper Sulfide Nanoparticles and Hollow Gold Nanospheres on Degradability and Toxicity. *ACS Nano* **2013**, *7*, 8780–8793.

(44) Liu, G.; Gao, J. H.; Ai, H.; Chen, X. Y. Applications and Potential Toxicity of Magnetic Iron Oxide Nanoparticles. *Small* **2013**, *9*, 1533–1545.

(45) Hao, R.; Xing, R. J.; Xu, Z. C.; Hou, Y. L.; Gao, S.; Sun, S. H. Synthesis, Functionalization, and Biomedical Applications of Multifunctional Magnetic Nanoparticles. *Adv. Mater.* **2010**, *22*, 2729–2742.

(46) Wang, A. Y.; Kuo, C. L.; Lin, J. L.; Fu, C. M.; Wang, Y. F. Study of Magnetic Ferrite Nanoparticles Labeled with ^{99m}Tc -pertechnetate. *J. Radioanal. Nucl. Chem.* **2010**, *284*, 405–413.

(47) Wu, H. X.; Liu, G.; Zhuang, Y. M.; Wu, D. M.; Zhang, H. Q.; Yang, H.; Hua, H.; Yang, S. P. The Behavior after Intravenous Injection in Mice of Multiwalled Carbon Nanotube/ Fe_3O_4 Hybrid MRI Contrast Agents. *Biomaterials* **2011**, *32*, 4867–4876.

(48) Song, X. J.; Gong, H.; Yin, S. N.; Cheng, L.; Wang, C.; Li, Z. W.; Li, Y. G.; Wang, X. Y.; Liu, G.; Liu, Z. Ultra-Small Iron Oxide Doped Polypyrrole Nanoparticles for *in Vivo* Multimodal Imaging Guided Photothermal Therapy. *Adv. Funct. Mater.* **2014**, *24*, 1194–1201.

(49) Wang, C.; Xu, H.; Liang, C.; Liu, Y. M.; Li, Z. W.; Yang, G. B.; Cheng, L.; Li, Y. G.; Liu, Z. Iron Oxide@Polypyrrole Nanoparticles as a Multifunctional Drug Carrier for Remotely Controlled Cancer Therapy with Synergistic Antitumor Effect. *ACS Nano* **2013**, *7*, 6782–6795.

(50) Tian, Q. W.; Wang, Q.; Yao, K. X.; Teng, B. Y.; Zhang, J. Z.; Yang, S. P.; Han, Y. Multifunctional Polypyrrole@ Fe_3O_4 Nanoparticles for Dual-Modal Imaging and *in Vivo* Photothermal Cancer Therapy. *Small* **2014**, *10*, 1063–1068.

(51) Lin, M.; Guo, C. R.; Li, J.; Zhou, D.; Liu, K.; Zhang, X.; Xu, T. S.; Zhang, H.; Wang, L. P.; Yang, B. Polypyrrole-Coated Chainlike Gold Nanoparticle Architectures with the 808 nm Photothermal Transduction Efficiency up to 70%. *ACS Appl. Mater. Interfaces* **2014**, *6*, 5860–5868.

(52) Huang, P.; Lin, J.; Li, W. W.; Rong, P. F.; Wang, Z.; Wang, S. J.; Wang, X. P.; Sun, X. L.; Aronova, M.; Niu, G.; Leapman, R. D.; Nie, Z. H.; Chen, X. Y. Biodegradable Gold Nanovesicles with an Ultrastrong Plasmonic Coupling Effect for Photoacoustic Imaging and Photothermal Therapy. *Angew. Chem., Int. Ed.* **2013**, *52*, 13958–13964.

(53) Song, J. B.; Zhou, J. J.; Duan, H. W. Self-Assembled Plasmonic Vesicles of SERS-Encoded Amphiphilic Gold Nanoparticles for Cancer Cell Targeting and Traceable Intracellular Drug Delivery. *J. Am. Chem. Soc.* **2012**, *134*, 13458–13469.

(54) Wang, S. T.; Chen, K. J.; Wu, T. H.; Wang, H.; Lin, W. Y.; Ohashi, M.; Chiou, P. Y.; Tseng, H. R. Photothermal Effects of

Supramolecularly Assembled Gold Colloids for Targeted Treatment of Cancer Cells. *Angew. Chem., Int. Ed.* **2010**, *49*, 3777–3781.

(55) Yang, C. H.; Sui, H. Y.; Li, X. W.; Han, J. S.; Luo, X. T.; Zhang, H.; Sun, H. Z.; Sun, H. C.; Zhou, Y. M.; Yang, B. Gold Nanoparticle Superstructures with Enhanced Photothermal Effect. *CrystEngComm.* **2013**, *15*, 3490–3497.

(56) Sun, S. H.; Zeng, H. Size-Controlled Synthesis of Magnetite Nanoparticles. *J. Am. Chem. Soc.* **2002**, *124*, 8204–8205.

(57) Zhang, X.; Lin, M.; Lin, X. Y.; Zhang, C. T.; Wei, H. T.; Zhang, H.; Yang, B. Polypyrrole-Enveloped Pd and Fe_3O_4 Nanoparticle Binary Hollow and Bowl-Like Superstructures as Recyclable Catalysts for Industrial Wastewater Treatment. *ACS Appl. Mater. Interfaces* **2014**, *6*, 450–458.

(58) Bai, F.; Wang, D. S.; Huo, Z. Y.; Chen, W.; Liu, L. P.; Liang, X.; Chen, C.; Wang, X.; Peng, Q.; Li, Y. D. A Versatile Bottom-up Assembly Approach to Colloidal Spheres from Nanocrystals. *Angew. Chem., Int. Ed.* **2007**, *46*, 6650–6653.

(59) Zhuang, J. Q.; Wu, H. M.; Yang, Y. G.; Cao, Y. C. Controlling Colloidal Superparticle Growth through Solvophobic Interactions. *Angew. Chem., Int. Ed.* **2008**, *47*, 2208–2210.

(60) Cornell, R. M.; Schwertmann, U. *The Iron Oxide: Structure, Properties, Reactions, Occurrences and Uses*; WILEY-VCH Verlag GmbH & Co. KGaA: Weinheim, Germany, 2003; pp 111–138.

(61) Zhao, Y.; Pan, H.; Lou, Y.; Qiu, X.; Zhu, J.; Burda, C. Plasmonic Cu_{2-x}S Nanocrystals: Optical and Structural Properties of Copper-Deficient Copper(I) Sulfides. *J. Am. Chem. Soc.* **2009**, *131*, 4253–4261.

(62) Roper, D. K.; Ahn, W.; Hoepfner, M. Microscale Heat Transfer Transduced by Surface Plasmon Resonant Gold Nanoparticles. *J. Phys. Chem. C* **2007**, *111*, 3636–3641.

(63) Tian, Q. W.; Jiang, F. R.; Zou, R. J.; Liu, Q.; Chen, Z. G.; Zhu, M. F.; Yang, S. P.; Wang, J. L.; Wang, J. H.; Hu, J. Q. Hydrophilic Cu_9S_5 Nanocrystals: A Photothermal Agent with a 25.7% Heat Conversion Efficiency for Photothermal Ablation of Cancer Cells *in Vivo*. *ACS Nano* **2011**, *5*, 9761–9771.

(64) Hessel, C. M.; Pattani, V. P.; Rasch, M.; Panthani, M. G.; Koo, B.; Tunnell, J. W.; Korgel, B. A. Copper Selenide Nanocrystals for Photothermal Therapy. *Nano Lett.* **2011**, *11*, 2560–2566.